ACS APPLIED MATERIALS & INTERFACES

Research Article

www.acsami.org

Resilient Energy Storage under High-Temperature with In-Situ-Synthesized MnO_x@Graphene as Anode

Xiaodong Tian,[†,‡] Hongli Zhu,[*,§] Chan Jiang,[∥] Mingbao Huang,[†,‡] Yuanfu Deng,[†,‡] and Songping Wu[*,†,‡]

[†]School of Chemistry and Chemical Engineering, South China University of Technology, Guangzhou, 510641, China

[‡]Guangdong Key Laboratory of Fuel Cell Technology, Guangzhou 510641, China

[§]Department of Mechanical and Industrial Engineering, Northeastern University, Boston, Massachusetts 02115, United States

[∥]Department of Environmental Monitoring, Guangdong Polytechnic of Environmental Protection Engineering, Foshan, 528216, China

Supporting Information

ABSTRACT: An novel exfoliation strategy to few-layered graphene (FLG) combined with in situ synthesized amorphous MnO_x has been established via a facile and robust ball milling route in the presence of $KMnO_4$. The facile synthesis approach has the features of low cost, environmentally friendly nature and scalable capability. As an anode for lithium-ion batteries, amorphous MnO_x@FLG delivered a wonderful electrochemical performance under extremely operational conditions, that is, an excellent reversible capacity of 856 mAh g^{-1} at a high current density of 1 A g^{-1} after 75 cycles under a high temperature of 85 °C. Those excellent electrochemical performances could be ascribed to elaborately designed three-dimensional nanostructure, the well-chosen electrolyte, significant incorporation of in situ Mn(IV) nanocrystal and few-layered graphene, and the contribution of pseudocapacitance. Remarkable electrochemical performance under a widely operational temperature window makes the amorphous MnO_x@FLG composites promising anode of Li-ion batteries for heavy-duty application.

KEYWORDS: *in-situ exfoliation, few-layered graphene, amorphous, lithium-ion battery, harsh environment*

INTRODUCTION

Rechargeable lithium ion batteries (LIBs) have established themselves as dominant roles in portable electronic devices and electric vehicles (EVs).[1−3] Conventional anode material of graphite cannot meet the urgent demands for heavy-duty applications because of the low theoretical capacity of 372 mAh g^{-1}. Transition metal oxides (TMOs, M = Mn, Ni, Cu, Fe, Co) have been extensively exploited as promising anode materials.[4−7] Among them, manganese oxides were proved to be attractive choices because of their high theoretical capacity, low potential, high abundance and environmental benignity.[8] However, successful implementation of manganese oxides has been hindered by drastic volume changes and low electronic conductivity, which have resulted in poor cycling stability and inferior rate capability.[9,10] To settle those issues, artificial formation of amorphous structure appears to be an effective strategy since the amorphous framework will be less structural confinement than crystalline materials during the lithiation/delithiation.[11−13] Accordingly, introduction of advanced carbon materials to amorphous manganese oxides is of great importance in constructing designed hybrid structure to achieve the aim of further enhancing electrochemical performance. In previous references, MnO_x/ordered mesoporous carbon,[14] amorphous MnO_x−C nanoparticles,[15] MnO_x/C nanocomposites,[16] and MnO_x/SWCNTs[17] delivered reversible capacities of 996 mAh g^{-1} at 50th cycle, ∼650 mAh g^{-1} accompanied by a capacity retention of 93% after 130 cycles, ∼500 mAh g^{-1} for 100 cycles at a current density of 200 mA g^{-1}, and 850 mAh g^{-1} at 100 mA g^{-1} after 36 cycles, respectively. Recent continuous research, such as TiO_2-doped MnO_x composites[18] and MnO_x@carbon hybrid nanowire,[19] have garnered the similar electrochemical response.

Obviously, aforementioned investigations have demonstrated the potential application for MnO_x-based materials in LIBs so far. However, emerging large-power applications, such as electric vehicles and static energy storage stations, strongly

Received: July 7, 2017
Accepted: September 12, 2017
Published: September 12, 2017

DOI: 10.1021/acsami.7b09853
ACS Appl. Mater. Interfaces 2017, 9, 33896−33905

Scheme 1. Schematic Illustration of the Exfoliation Process for Graphite under Wet Ball-Milling Condition

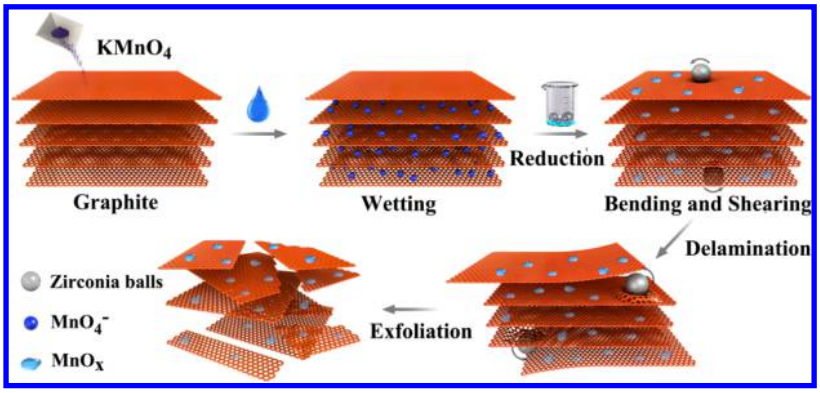

call for super batteries. For EVs, electrical energy storage devices need to successfully endure temperatures of least at 60 °C, which is a serious burden for existing technologies.[20] The addition of a cooling system increases the overall cost of the electronics and lowers the energy density of the EVs.[21] Consequently, excellent electrochemical performances for amorphous MnO_x-based materials under harsh operational conditions such as widely operational temperature region and large-current density were actually appealing goals for satisfying the urgent requirement of heavy-duty applications. Therefore, investigations into high-temperature performance and mechanism of A-MnO_x/carbon composites are highly desirable, and more arduous efforts need to be paid before the actual application becomes possible for the special material system.

Herein, we first reported a robust ball milling method for large-scalable fabrication of amorphous MnO_x@few-layered graphene (A-MnO_x@FLG) based on the recent investigations.[22] During this process, the graphite was exfoliated into few-layered graphene, which built up highly electronically conductive matrix. A-MnO_x@FLG could be effectively operated under high temperature of 85 °C, rendering outstanding high-temperature performance of 856 mAh g^{-1} after 75 cycles at 1 A g^{-1}. Such an excellent performance was the result of elaborately designed three-dimensional nanostructure, the well-chosen electrolyte, gradual emergence of Mn(IV) nanocrystal induced by reaction kinetics and contribution of capacitive charge storage. We believe that our works possess obvious features as compared with recent literatures, that is, (1) novel, scalable synthesis method, (2) remarkable high-temperature performance, and (3) in-depth investigation into high temperature mechanism. Those remarkable attributes enable A-MnO_x@FLG to be promising anode materials for power batteries.

EXPERIMENTAL METHODS

Synthesis of A-MnOx@FLG. An unique exfoliation technology of graphite layer with high-energy ball milling approach assisted by strong oxidant was adopted to achieve large-scalable fabrication of in situ amorphous MnO_x@few-layered graphene nanocomposites (A-MnO_x@FLG). As a typical sample, 3 g of graphite and 12 g of potassium permanganate ($KMnO_4$) were dispersed in 50 mL of water with a 5:1 mass ratio of zirconia balls to the whole raw material for 48 h by a speed of rotation of 400 rpm. When the reaction finished, the product was filtered and then washed four times with distilled water to remove potassium-containing compounds,[23] finally dried at 60 °C for 12 h to yield A-MnO_x@FLG.

Characterization. X-ray diffraction (XRD) patterns were collected through D8 Advance (Bruker AXS, Germany) with Cu Kα (λ = 0.15406 nm) radiation with an accelerating voltage of 40 kV and a generator current of 40 mA. Raman spectrometer was implemented to gain the Raman spectrum for the active materials (LabRAM Aramis, HJY, France). Elemental compositions and the valence of individual element in electrochemically active materials were explored by X-ray photoelectron spectroscope (XPS, Kratos Axis Ultra DLD, Japan). Transmission electron microscope (TEM) and high-resolution TEM (HRTEM) images were gathered with JEM-2100HR electron microscope (JEOL, Tokyo, Japan) at an accelerating voltage of 200 kV. Nitrogen adsorption−desorption isotherm measurements (3H-2000PS1, Baishide Co., Beijing, China) conducted at 77 K provided data about Brunauer−Emmett−Teller (BET) surface area and porosity. Infrared absorption spectra were measured to extract key characteristic parameters of particles (Bruker Tensor 27, Germany). The amount of carbon in A-MnO_x@FLG was probed by Thermogravimetric analysis (TGA) with a temperature ranging from 30 to 800 °C at a heating rate of 10 °C min^{-1} in air (Q600 SDT, TA INC, American).

Electrochemical Measurements. Coin-type half-cells (CR2016) were assembled in an argon-filled glovebox. Coating process was employed to make work electrodes loaded on a Cu foil with mixtures containing active materials, polyvinylidene fluoride and acetylene black with a mass ratio of 8:1:1. And counter electrode was a lithium foil. The separator films were commercial available (Celgard, North Carolina, USA). The electrolyte was a solution of 1 mol L^{-1} $LiPF_6$ in designed solvents of ethylene carbonate and ethyl methyl carbonate (30:70 by volume) with the additives of vinylene carbonate (1.5%) and propylene sulphite (1%). Galvanostatic charge/discharge measurements were operated with battery test system (Neware, BTS2300, Shenzhen, China) ranging from 0.01 to 3 V. Electrochemical workstation (CHI 660E, Chenhua, Shanghai, China) was adopted to gain cyclic voltammetry (CV) and electrochemical impedance spectroscope (EIS) signals. The potential for CV ranged from 0 to 3.0 V at a scan rate of 0.5 mV s^{-1}, and EIS were measured in the frequency range of 0.01 Hz−100 kHz. Note that specific capacities were calculated based on A-MnO_x@FLG nanoparticles.

RESULTS AND DISCUSSION

Graphite layers were here massively exfoliated with high-energy ball milling route in the presence of $KMnO_4$ to gather nanoparticles comprising of exfoliated few-layered graphene and in situ synthesized amorphous MnO_x. Such a route has presented some remarkable features of interest. Nature graphite is allowed to undergo cooperative binding in the small area beneath the balls during the wet-milling process,[22] distinctively making the out-of-plane displacement of each graphite layer. The displacement enables $KMnO_4$ solution to easily infiltrate into the microwrinkling with capillary force, whereby MnO_x is in situ synthesized via reduction of $KMnO_4$ by graphite. Simultaneously, local pinning in the binding area is accordingly formed with the help of powerful shear force. The results increase the interfacial commensurability, further greatly improve static friction. As a result, nature graphite integrated

DOI: 10.1021/acsami.7b09853
ACS Appl. Mater. Interfaces 2017, 9, 33896−33905

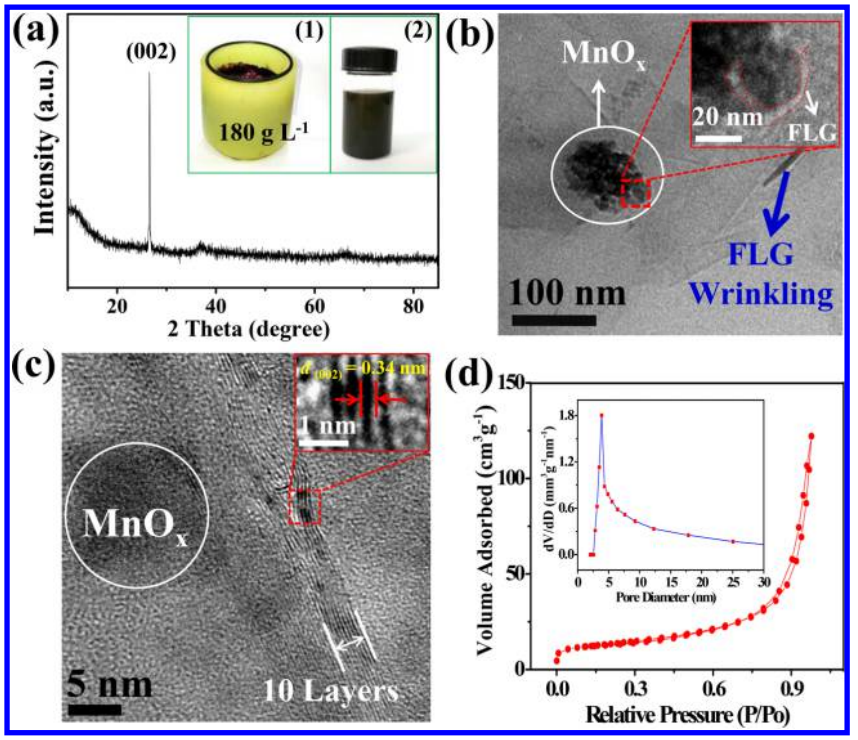

Figure 1. (a) XRD profile of A-MnO_x@FLG. Inset 1: A jar with zirconia balls and products. Inset 2: Product dispersed in water with a concentration of 1 mg mL^{-1}. (b) Typical TEM image of A-MnO_x@FLG. Inset is the enlarged part marked with red dotted frame. (c) HRTEM image of A-MnO_x@FLG. Inset is the HRTEM image of few-layered graphene. (d) Nitrogen adsorption−desorption isotherms of A-MnO_x@FLG. Inset is the corresponding pore size distribution curve of resultant A-MnO_x@FLG.

with *in situ* $MnO_x$was successfully exfoliated by constant shear, collecting scalable A-MnO_x@FLG nanoparticles (Scheme 1).

As illustrated in Figure 1a, XRD profile of amorphous MnO_x@FLG suggested the obvious existence of graphite (PDF No. 41-1487) with a characteristic diffraction peak of (002) at 26.6°. No diffraction peaks of crystalline manganese oxide could be perceived for an observer, indicating the amorphous nature of the MnO_x in this composite. In addition, scalable capability of 180 g L^{-1} and remarkable dispersibility were also depicted in inset 1 and 2 in the Figure 1a, respectively, revealing that such a method is readily scaled up for practical industrial application. The morphology and structure of the A-MnO_x@FLG were investigated by TEM (Figure 1b). The almost transparent graphite sheets could be explicitly recognized, whereby we deduced an explicit fact that layer numbers of graphite have been greatly reduced via the robust ball milling in the presence of $KMnO_4$. Further investigation showed that A-MnO_x nanoparticles were fully covered by few-layered graphene nanosheets (marked with red in inset in Figures 1b and S1). The exfoliated graphite with ∼10 vertical graphene layers have been observed in high magnification TEM image (Figure 1c), where interplanar spacings of 0.34 nm (inset in Figure 1c) readily responded to (002) plane for graphite. Amorphous nature of MnO_x with irregular particle size of ∼8 nm was also verified due to the absence of obvious crystal lattice. The specific surface area of A-MnO_x@FLG characterized by nitrogen adsorption and desorption isotherms at 77 K displayed the isothermal plot of the amorphous MnO_x/graphene hybrid (Figure 1d), which was a typical type IV isotherm representing a mesoporous structure with a BET specific surface area as high as 45.3 m^2 g^{-1}. The pore size distribution may be indicative of numerous mesopores with ∼2.8 and 8.5 nm in diameter for corresponding product (inset of Figure 1d), in coincidence with the TEM observations.

A sharp peak of G band at 1570 cm^{-1} in Raman spectra of the A-MnO_x@FLG indicated that the ordered sp^2 bonded carbon dominated the structure (Figure 2a). Peaks at 558 and 631 cm^{-1} (Figure 2b) were assigned to the vibration of Mn−O, standing for the existence of MnO_x.[24,25] In previous reference, the intensity ratio of Raman D/G band was proportional to inverse nanosheet length,[26] hence intensity ratio of 0.48 for D/G band implied the reduced size of graphene nanosheets (Figure 2c), which was confirmed by Raman spectrum of graphite (Figure S2), as well as the SEM image of nature graphite (Figure S3a) and TEM image of A-MnO_x@FLG (Figure S3b). Similarly, introduction of basal-plane defects to graphene nanosheets during ball-milled exfoliation assisted by $KMnO_4$ has given rise to ∼8.9 of D/D′ band intensity ratio (Figure 2c).[27,28]

The oxidation state x in the amorphous MnO_x was determined by X-ray photoelectron spectroscopy (XPS) measurements. The peaks caused from Mn (3p, 3s, $2p_{1/2}$, and $2p_{3/2}$) and O (1s) in the survey of XPS spectrum could be assigned to MnO_x (Figure 3a). The high-resolution C 1s spectrum was showed in Figure 3b. We could attribute the large peak at 284.5 eV to graphite carbon (C−C), and a weak peak at 286.2 eV to C−O bond, respectively. Oxygen 1s peaks were carefully divided into two simulative signals at 529.8 and 532.0 eV (Figure 3c), assigned to the oxygen bonded with manganese and slight oxidation of graphite sheets,[29,30] respectively. Carbon spectrum and oxygen spectrum appeared to propose the slight oxidation of exfoliated few-layered graphene when $KMnO_4$ was served as oxidant as well as Mn source during ball-milled exfoliation. High-resolution XPS analysis was utilized to explore the valence states of the Mn (Figure 3d). The peaks of Mn

DOI: 10.1021/acsami.7b09853
ACS Appl. Mater. Interfaces 2017, 9, 33896−33905

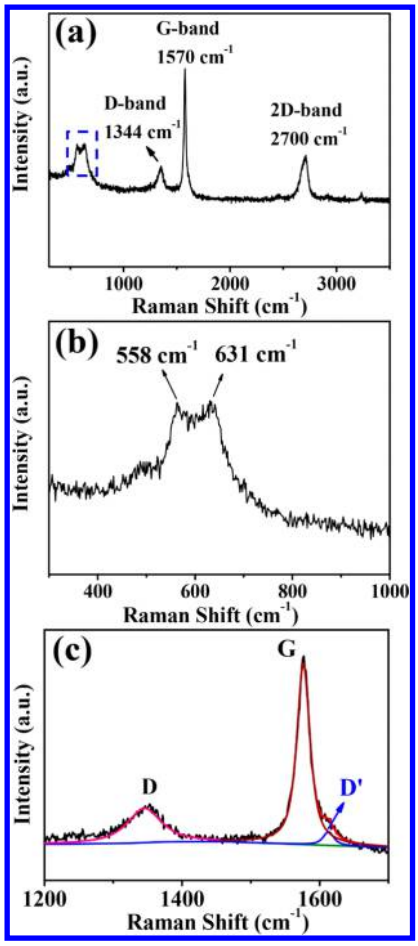

Figure 2. Raman spectra of A-MnO_x@FLG: (a) Survey spectrum, (b) with range from 300 to 1000 cm^{-1}, and (c) with range from 1200 to 1700 cm^{-1}.

$2p_{1/2}$ and $2p_{3/2}$ could be decomposed into two groups, respectively. Two signals at 641.2 and 652.8 eV may be indexed to Mn(II),[31] while the peaks at 642.4 and 654.1 eV corresponded to Mn (III).[32] The simulating result of XPS spectra constructively manifested that amorphous MnO_x consisted of 32.5 mol % Mn^{2+} and 67.5 mol % Mn^{3+}, respectively, whereby the average oxidation state of manganese in amorphous MnO_x could be reasonably evaluated as $x = 1.34$. Thermogravimetric analysis (TGA) exhibited that there existed 40.8 wt % of carbon content in the A-MnO_x@FLG composites (Figure S4). On the basis of Raman spectra, FT-IR (Figure S5), XPS and TG analysis, emergence of A-MnO_x@FLG nanocomposites have been solidly confirmed. Therefore, the above-mentioned observations have given strong evidence of successful fabrication of A-MnO_x@FLG nanocomposites via a one-step and scalable high-energy ball-mill route assisted by $KMnO_4$ at ambient temperature. As synthesized A-MnO_x@FLG featured well-exfoliated few-layered graphene and in situ synthesized amorphous MnO_x nanoparticles.

As reported in refs 14 and 19, MnO_x-based materials have widely investigated as anode electrode for LIBs operated under ambient temperature, exhibiting that MnO_x-based materials possessed significant potential to deal with the daily use.[33,7,8] However, more harsh application environment need to be seriously faced because Li-ion batteries containing A-MnO_x@FLG may be utilized in some extreme fields such as space exploration, extremely environmental adventure, volcanic observation and so on.[34] Unfortunately, relevant researches are rarely for oxide-based anode materials to date. Therefore, in-depth exploration of electrochemical response capability for A-MnO_x@FLG under high-temperature becomes of great importance and actual emergency.

To form stable SEI under high temperature, we have elaborately chosen electrolyte additive, that is, vinylene carbonate and propylene sulfite. As reported by Mao et al.,[35] the sulfite-containing additive gave rise to stable cycling

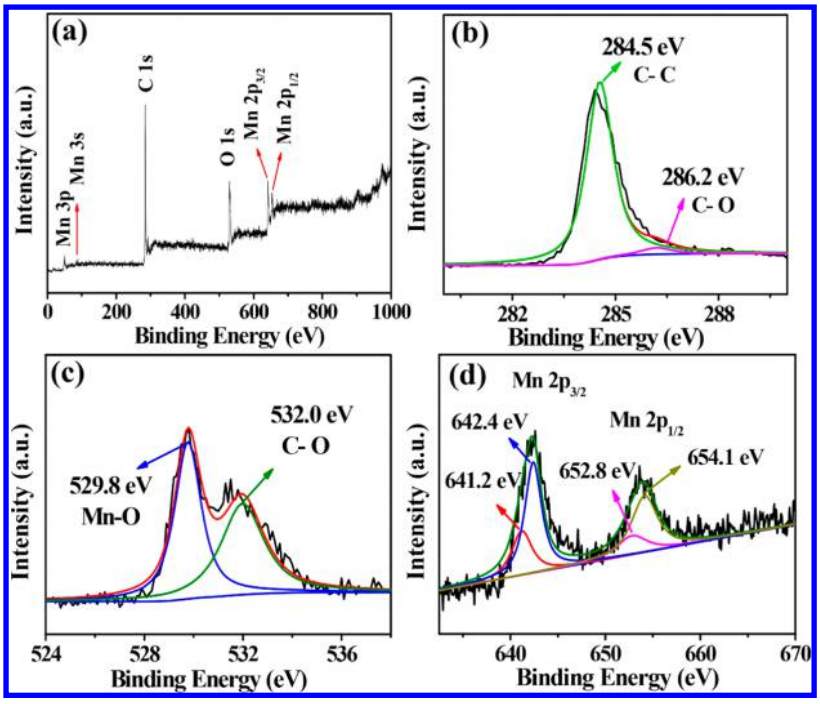

Figure 3. XPS spectra for (a) survey, (b) C 1s, (c) O 1s, (d) Mn 2p of A-MnO_x@FLG.

DOI: 10.1021/acsami.7b09853
ACS Appl. Mater. Interfaces 2017, 9, 33896−33905

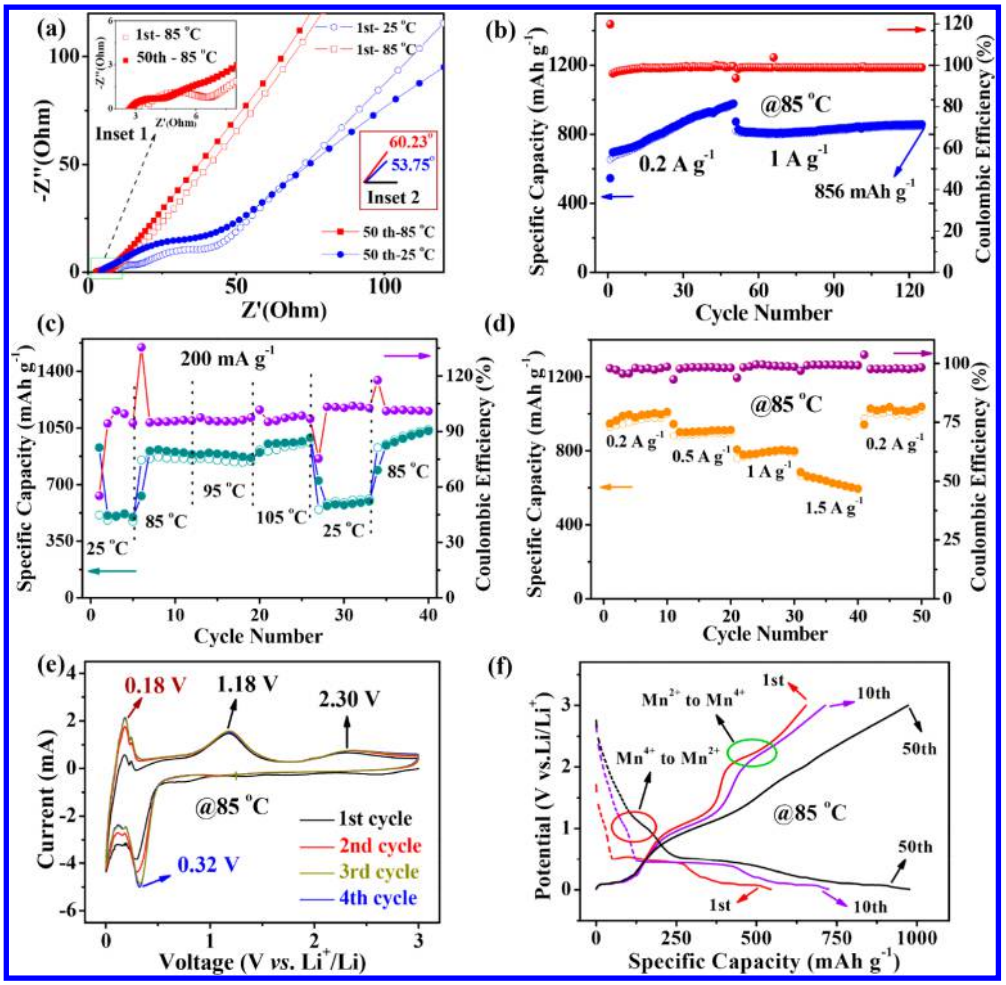

Figure 4. (a) Nyquist plots of A-MnO_x@FLG hybrid measured at the temperature 25 and 85 °C, respectively, after 1 and 50 cycles at room temperature. Inset 1: Enlargement of green frame. Inset 2: Slope lines in low frequency region under 25 and 85 °C for the first discharge/charge, respectively. (b) Cycling performance and columbic efficiency of the A-MnO_x@FLG at 85 °C after being activated for 5 cycles at the room temperature, respectively. (c) The specific capacity of A-MnO_x@FLG under different temperatures at a current density of 200 mA g^{-1}. (d) Rate performance of the prepared A-MnO_x@FLG at 85 °C. (e) Cyclic Voltammograms of the A-MnO_x@FLG electrodes at 0.5 mV s^{-1} under 85 °C. (f) Galvanostatic discharge and charge curves at the first, 10th and 50th for electrodes operated under a current density of 200 mA g^{-1} at 85 °C after being activated for 5 cycles.

performance at 60 °C, where vinylene carbonate was considered as the most effective additive.[36] We believed that elaborately chosen electrolyte was an important factor for enhanced electrochemical performance for corresponding electrode.

To better understand the different electrochemical features of A-MnO_x@FLG electrode under different temperature windows, EIS of electrode cycled at a current density of 200 mA g^{-1} was measured at two typical temperature points, that is, 25 and 85 °C (Figure 4a). After the first cycle, the significant small radius of semicircle measured at the 85 °C was observed to occur in the high frequency region of EIS plot, suggesting that A-MnO_x@FLG hybrid showed a decreased charge transfer resistance (R_{ct}) at 85 °C based on equivalent circuit diagram (Figure S6 and Table S1). Notably, merged resistance of R_{sf+ct} decreased to 1.77 Ω at 50th cycle under 85 °C from 3.29 Ω at first cycle (inset 1 in Figure 4a and Table S1), suggesting that high conductivity of electrode has appeared after 50 cycles. In a low frequency region, 60.23° of line slope at EIS plots under 85 °C could be perceived (inset 2 in Figure 4a), higher than that of 53.75° yielded in room temperature, implying faster Li^+ diffusion and strengthened capacitive-like behavior.[37] Those enhanced electrochemical behaviors, i.e., reduced resistance, fast Li^+ diffusion and improved capacitive-like performance under high temperature, were still perfectly maintained after 50 cycles. In fact, we have reported that several materials, such as FeS_2,[38] MnO@$MnFe_2O_4$,[39] and Co_9S_8[40] possessed a powerful capability in providing enhanced electrochemical performance under high temperature. Motivated by this enhanced kinetics, we drew much attention to other electrochemistry behaviors, and looked forward to discovering further amazing performance for A-MnO_x@FLG.

It is much in evidence that operational temperatures have explicitly exercised subtle influence over the conductivity of corresponding electrodes made of A-MnO_x@FLG, whose temperature-dependent performances were deeply investigated to highlight their superior electrochemical feature (Figure 4b). A-MnO_x@FLG electrodes were activated for 5 cycles at room temperature, with an initial Columbic efficiency of 57%. Subsequently, the electrode afforded a reversible capacity of 654 mAh g^{-1} at the first cycle and 973 mAh g^{-1} at the 50th cycle at 85 °C under a current density of 0.2 A g^{-1}, with an increasing capacity of 6.46 mAh g^{-1} per cycle, giving an almost 100% Columbic efficiency upon each cycle. The increasing

DOI: 10.1021/acsami.7b09853
ACS Appl. Mater. Interfaces 2017, 9, 33896−33905

trend was due to the improved electrochemistry kinetics (above-mentioned increased conductivity) during cycling and the gradual emergence of Mn(4+) derived from electrochemical reaction according to the references.[7,41] Subsequently, A-MnO_x@FLG electrode was operated at a large current density of 1.0 A g^{-1}, rendering a discharge capacity of 856 mAh g^{-1} after 75 discharge/charge cycles, with a capacity retention of 105%. Interestingly, A-MnO_x@FLG materials could be cycled at a current density of 1−1.5 A g^{-1}, exhibiting an excellent long-term cycling stability (Figure S7). The high-temperature performance has also been observed in other materials such as red phosphorus-graphene nanosheets,[42] $Li_4Ti_5O_{12}$−TiO_2 hybrid[43] and our previous works.[38−40] More importantly, the reversible capacity of cells could be recovered, that is, ∼650 mAh g^{-1} at a current density of 0.2 A g^{-1}, after they have undergone such severe temperature environments. As intriguing comparisons, A-MnO_x@FLG electrode rendered a remarkable reversible capacity of 1012 mAh g^{-1} after 300 cycles under a current density of 200 mA g^{-1} at room temperature (Figure S8) and an average charge capacity of 80.7 mAh g^{-1} after 50 cycles at a current density of 50 mA g^{-1} even at temperature of −25 °C (Figure S9).

Influence of operational temperature on electrochemical performance of A-MnO_x@FLG electrode has been further investigated at a current density of 200 mA g^{-1} (Figure 4c). As the temperature increased from 25 to 85 °C, reversible capacity of MnO_x@FLG has significantly increased owing to the enhanced electrochemical behaviors at high temperature. However, when the temperature exceeded 85 °C, the capacity change became unobvious. After operated at 105 °C for 7 cycles, the reversible capacity of 611 mAh g^{-1} could be successfully recovered as electrode was operated at ambient temperature. Considering practical application and boiling point of solvent in electrolyte, we elaborately chose the 85 °C as the typical temperature point in our study.

After 50 cycles under 85 °C at a current density of 200 mA g^{-1}, rate performance of the A-MnO_x@FLG electrode was further investigated (Figure 4d), delivering an average capacity of 961 mAh g^{-1} at a low rate of 0.2 A g^{-1}. Subsequently, the electrode still possessed a robust capability in retaining an average reversible capacity of 627 mAh g^{-1} even at a high current density of 1.5 A g^{-1}. After rapid discharge/charge, a reversible capacity of 998 mAh g^{-1} could be recovered when a current density backed to 0.2 A g^{-1}, being indicative of a wonderful electrochemical reversibility at elevated temperature.

Above results have demonstrated that A-MnO_x@FLG possessed remarkable electrochemical performance under 85 °C, that is, reversible capacity of 973 mAh g^{-1} at 50th cycle at a current density of 0.2 A g^{-1} and 856 mAh g^{-1} at 1 A g^{-1} after next 75 cycles under a high temperature of 85 °C. The origination of the excellent electrochemical performance has aroused our much attention.

Cyclic voltammetry (CV) was adopted to understand the root cause of superior electrochemical performance of A-MnO_x@FLG under high temperature of 85 °C (Figure 4e). The CV profiles have showed intriguing and attractive characterizes to a careful observer. In the first cathodic cycle, a reduction peak at 0.29 V (Figure S10) would be attributed to the reduction of Mn element from higher oxidation state to lower oxidation state such as Mn(0),[33] and the formation of SEI film.[15] It was perceived to upshift to 0.32 V in the succedent cycles. In the anodic scan, a sharp peak observed at 0.18 V would be ascribed to deintercalation of lithium ions between graphite layers. A broad oxidation peak at 1.18 V could define itself as the result of oxidation of metallic Mn to Mn^{2+}.[8] Interestingly, an oxidation peak at ∼2.30 V has grown to a distinguishable level even at the first cycle. More importantly, it finally became stable when electrodes were sequentially operated after 50 cycles (Figure S10), suggesting that the electrochemically synthesized Mn^{4+} appeared to be reversible during Li-cycling. As a strong contrast, such an oxidation was previously expected to gradually occur after 150 cycles under ambient temperature (inset in Figure S11).

There exist two intriguing features in the CV profile. (1) The improved Li-reaction kinetics motivated by heat energy would enormously accelerate reaction speed of electrochemical oxidation, leading to the early emergence of Mn(0) in cathodic scanning and Mn^{4+} in anodic sweep. (2) It is of great importance to note that almost unchangeable potential difference (ΔE) of ∼0.86 V ($\Delta E = E_{oxidation} - E_{reduction}$) collected at 85 °C is significant low (Figure 4e), as compared with that of 1.13 V at room temperature (Figure S11). Decreased potential difference signified the reduced polarization of the electrode,[44] which should reasonably result in an excellent reversibility and improved electrochemical performance.

To further expound electrochemical mechanism, galvanostatic discharge/charge cycling profiles of the A-MnO_x@FLG operated at 85 °C were examined at a current density of 0.2 A g^{-1} (Figure 4f). An explicitly observable plateau at 0.48 V in the first discharge process corresponded to the reduction of MnO_x to metallic Mn. In the first charge curve, a plateau at around 1.11 V could be considered as the consequence of the oxidation of metallic Mn to Mn^{2+}. An obvious plateau at 2.25 V would be apperceived, which could be ascribed to further oxidation of Mn^{2+} to Mn^{4+}, exactly agreeable with those in CV observation. An emerging platform at ∼1.04 V was of clear recognition in the subsequent discharge curves, where reduction of Mn^{4+} to Mn^{2+} has served itself as a contributor for the platform.[7] After 50 cycles, the charge plateaus at 2.25 V and the discharge plateaus at 1.04 V were nearly inclined in shape, implying a typical characteristic of double-layer capacitor.[45]

We further identify the capacitive contributions to the total capacity based on previously reported approach.[46−48] Cyclic voltammetry examinations for the A-MnO_x@FLG were carried out to analyze the electrochemical transport kinetics with varying sweep rates at the high temperature of 85 °C (Figure 5a). The current response (i) at a fixed potential (V) was consisted of two parts, that is, diffusion-controlled insertion ($k_2\nu^{1/2}$) and capacitive effects ($k_1\nu$).[49] Owing to that k_1 and k_2 are fixed at specific potentials, we should utilize the currents at different sweep rates to calculate the k_1 and k_2 according to the equation $i(V) = k_1\nu + k_2\nu^{1/2}$, where ν is the sweep rate. Thereby, it is quite possible to make a distinction between diffusion-controlled Faradaic intercalation and capacitive process at a specific potential.

The capacitive current was showed at a sweep rate of 0.1 mV s^{-1} at 85 °C (shaded region in Figure 5b), suggesting estimated 27.9% capacitive contribution to the total capacity. The separation of the capacitive effect and diffusion-controlled contribution were displayed in Figure 5c. The results depicted that the capacity contribution of capacitive behavior increased from 27.9% to 45.1% with sweep rate from 0.1 to 0.8 mV s^{-1}, which implied that capacitive charge storage played a significant role in the total capacity, especially at high scan rates. The high contribution of capacitive effect in our case might be ascribed to

DOI: 10.1021/acsami.7b09853
ACS Appl. Mater. Interfaces 2017, 9, 33896−33905

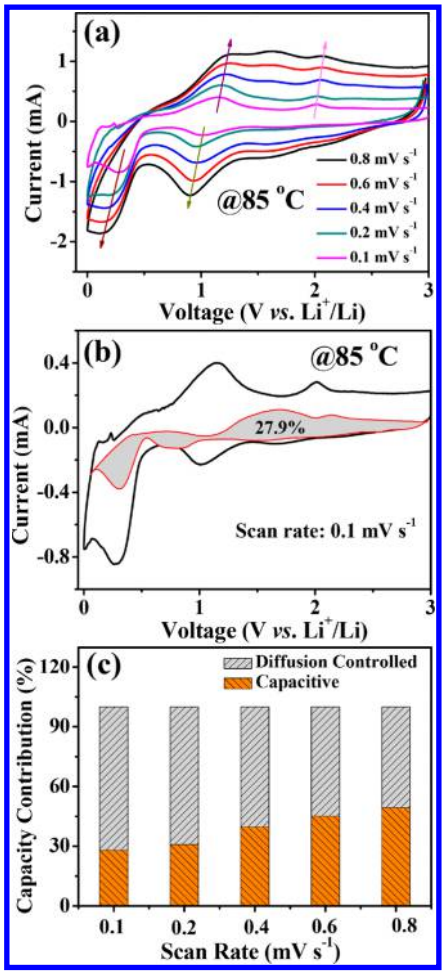

Figure 5. (a) CV curves of A-MnO_x@FLG at different scan rates ranging from 0.1 to 0.8 mV s^{-1} after 50 cycles under a current density of 0.2 A g^{-1} at 85 °C. (b) CV profile with the capacitive contribution to the total current shown by the shaded; (c) The capacity contribution at different scan rates.

the amorphous nature of MnO_x, which provided more cation/anion vacancies, void spaces, cluster gaps or interstitial sites for lithium storage.[50,51] The process about the calculation of capacity contributed by capacitive-controlled behaviors was shown in Figure S12. As a result, the root cause of increased capacity after 50 cycles would be not only the appearance of Mn (IV), but also the contribution of capacitive charge storage.

After 50 cycles under a current density of 200 mA g^{-1} under 85 °C, the morphology of active materials was detected by TEM images. As showed in Figure 6a and Figure S13a−13b, the charged active materials in A-MnO_x@FLG electrodes were strongly believed to have experienced an obviously chemical pulverization and structural rearrangement. Monodispersed regular crystal nanoparticles of about 2 nm, instead of amorphous particles, have uniformly anchored on carbon matrix, dispelling electrochemical agglomeration during charge/discharge. Interplanar spacing of 0.209 nm (the inset of Figure 6a) and the selected area electron diffraction (SAED) (Figure 6b) might imply the existence of MnO_2, agreeable with the results by above-mentioned CV and galvanostatic discharge/charge profiles. Crystal nanoparticles were also observed to appear in discharged active materials (Figure 6c and Figure S13c−13d), where appearance of metallic Mn grains has been affirmed by interplanar spacing of 0.213 nm (the inset of Figure 6c) and SAED profile (Figure 6d). It is worth noting that Figure 6d also showed the typical 6-fold symmetric diffraction spots, which is an important characteristic of few-layered graphene sheets.[52] Such a stable interconnected 3D nanostructure not only improves the electronic conductivity but also accommodates volume expansion. In brief, the amorphous MnO_x particles have electrochemically changed into corresponding crystal nanoparticles during lithiation/delithiation, leading to enhanced kinetics. In previous works, electrochemically synthesized MnO_2 has been affirmed by XPS.[7,8] We believed that this is the first TEM observation of electrochemically induced crystal transformation of MnO_x to MnO_2 based on MnO_x electrodes. Such a crystal change was also observed in amorphous vanadium oxide/molybdenum oxide.[11]

There exist several striking features in this work. (1) A facile, environmentally friendly route to A-MnO_x@FLG has been established, demonstrating a robust competence in providing a scalable preparation strategy to meet the rigorous requirement of possible industrial application. As reported in a recent reference,[53] increase in the electrode thickness effectively decrease the cost per kWh. As-prepared A-MnO_x@FLG possesses obvious advantages of high volumetric specific capacity (i.e., 1721 mAh cm^{-3} after 75 cycles at a current density of 1 A g^{-1}) as compared with the commercial graphite (Figure S14), allowing for more cathode materials loaded on current collector. As a result, low cost and large energy for LIBs were highly expected when A-MnO_x@FLG was utilized in power battery; (2) The improved Li-reaction kinetics and reduced polarization of the electrode led to enhanced reversible capacity and an excellent reversibility for corresponding electrodes under high temperature; (3) The capacity contribution of capacitive behavior played a significant role in the total capacity, especially at high scan rates; (4) Electrochemically synthesized nanocrystals were reconstructed and in situ anchored on elastic FLG network to maintain structural integrity for corresponding electrodes, effectively accommodating volume expansion and improving the electronic conductivity; (5) The well-designed electrolyte was believed to possess a robust capability in forming stable SEI films under high temperature, resulting in excellent electrochemical performance. As a consequence, A-MnO_x@FLG could be normally operated at ultrahigh temperature of 85 °C, delivering a superior reversible capacity of 856 mAh g^{-1} at a current density of 1.0 A g^{-1} after 75 cycles.

CONCLUSIONS

In summary, we have established a wet ball-milling process to synthesize A-MnO_x@FLG nanomaterials, which were subsequently utilized as advanced anode materials, rendering an outstanding high-temperature performance of 856 mAh g^{-1} for A-MnO_x@FLG after 75 cycles at 1 A g^{-1} under 85 °C. The remarkable high-temperature electrochemical characteristic of A-MnO_x@FLG could be ascribed to elaborately designed three-dimensional nanostructure, the well-chosen electrolyte, the emergence of Mn^{4+} and the contribution of capacitive effects. Significant incorporation between in situ electrochemically synthesized nanocrystal from amorphous MnO_x and few-layered graphene robustly accommodate volume expansion of active materials. Those distinct features make A-MnO_x@FLG promising anode materials for power battery at extreme conditions. And such a synthesis strategy has a great potential for easily large-scale implementation and can be extended to other lithium storage materials.

DOI: 10.1021/acsami.7b09853
ACS Appl. Mater. Interfaces 2017, 9, 33896−33905

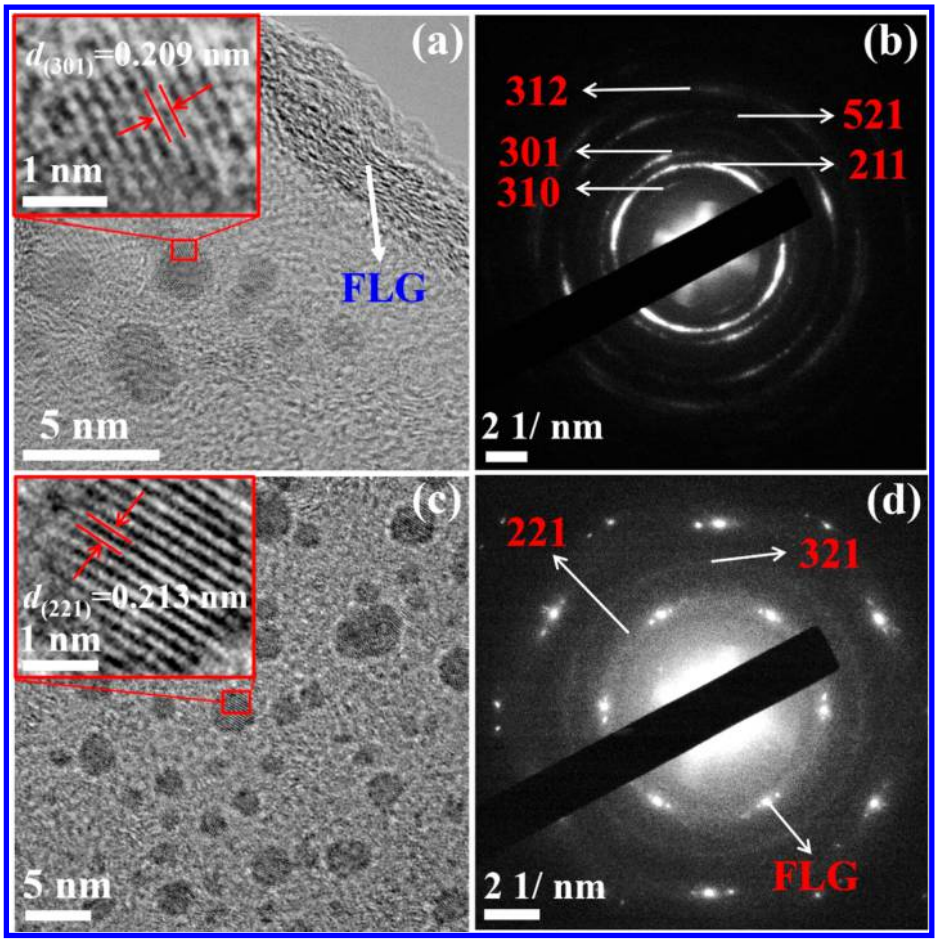

Figure 6. (a) HRTEM and (b) SAED images of electrode materials after 50 cycles at a current density of 200 mA g^{-1} under 85 °C in the fully charged state; (c) HRTEM, and (d) SAED images of electrode materials after 50 cycles at a current density of 200 mA g^{-1} under 85 °C in the fully discharged state.

■ ASSOCIATED CONTENT

Supporting Information

The Supporting Information is available free of charge on the ACS Publications website at DOI: 10.1021/acsami.7b09853.

TEM and SEM of A-MnO_x@FLG; Raman spectrum of graphite; SEM image of nature graphite and TEM image of A-MnO_x@FLG electrodes; thermogravimetric analysis; Fourier transform infrared spectroscopy (FTIR) of nature graphite and A-MnO_x@FLG, respectively; equivalent electrical circuit; fitting parameters of EIS at the 25 and 85 °C; cycling performance of A-MnO_x@FLG electrodes at the temperature of 85 °C; cycling performance at the room temperature; cycling performance at −25 °C; CV of the A-MnO_x@FLG electrodes after 50 cycles at 85 °C; CV of the A-MnO_x@FLG electrodes after 150 cycles at the room temperature; estimated capacitive current contribution at a scan rate of 0.2, 0.4, 0.6, and 0.8 mV s^{-1}; STEM and TEM images of electrode materials at 200 mA g^{-1} afer 50 cycles, under 85 °C; areal capacity and volumetric specific capacity of A-MnO_x@FLG electrodes (PDF)

■ AUTHOR INFORMATION

Corresponding Authors

*E-mail: umdenergyzhl@gmail.com (H.Z.).
*E-mail: chwsp@scut.edu.cn (S.W.).

ORCID

Yuanfu Deng: 0000-0002-2460-7224
Songping Wu: 0000-0002-4676-4925

Notes

The authors declare no competing financial interest.

■ ACKNOWLEDGMENTS

Dr. Wu acknowledges the Department of Science and Technology of Guangdong (Nos. 2014B010123001, 2015B090901030, and 2016B050502004), Guangzhou Science Technology and Innovation Commission (No. 2016201604030013), and Bureau of Science and Technology of Foshan Municipality (No. 2016AG100522), and the Guangzhou Scientific and Technological Planning Project (No. 201704030061).

■ REFERENCES

(1) Larcher, D.; Tarascon, J. M. Towards Greener and More Sustainable Batteries for Electrical Energy Storage. *Nat. Chem.* **2015**, *7* (1), 19−29.
(2) Nitta, N.; Wu, F.; Lee, J. T.; Yushin, G. Li-ion Battery Materials: Present and Future. *Mater. Today* **2015**, *18* (5), 252−264.
(3) Xue, D. J.; Xin, S.; Yan, Y.; Jiang, K. C.; Yin, Y. X.; Guo, Y. G.; Wan, L. J. Improving the Eectrode Performance of Ge through Ge@C Core-shell Nanoparticles and Graphene Networks. *J. Am. Chem. Soc.* **2012**, *134* (5), 2512−2515.

DOI: 10.1021/acsami.7b09853
ACS Appl. Mater. Interfaces 2017, 9, 33896−33905

(4) Ji, L.; Meduri, P.; Agubra, V.; Xiao, X.; Alcoutlabi, M. Graphene-based Nanocomposites for Energy Storage. *Adv. Energy. Mater.* **2016**, *6* (16), 1502159.
(5) Wu, H. B.; Chen, J. S.; Hng, H. H.; Lou, X. W. Nanostructured Metal Oxide-based Materials as Advanced Anodes for Lithium-ion Batteries. *Nanoscale* **2012**, *4* (8), 2526−2542.
(6) Guo, Y.-G.; Hu, J.-S.; Wan, L.-J. Nanostructured Materials for Electrochemical Energy Conversion and Storage Devices. *Adv. Mater.* **2008**, *20* (15), 2878−2887.
(7) Wang, S.; Xing, Y.; Xiao, C.; Xu, H.; Zhang, S. A Peapod-inspired MnO@C Core-shell Design For Lithium Ion Batteries. *J. Power Sources* **2016**, *307*, 11−16.
(8) Sun, Y.; Hu, X.; Luo, W.; Xia, F.; Huang, Y. Reconstruction of Conformal Nanoscale MnO on Graphene as a High-capacity and Long-life Anode Material for Lithium Ion Batteries. *Adv. Funct. Mater.* **2013**, *23* (19), 2436−2444.
(9) Lee, S. W.; Lee, C. W.; Yoon, S. B.; Kim, M. S.; Jeong, J. H.; Nam, K. W.; Roh, K. C.; Kim, K. B. Superior Electrochemical Properties of Manganese Dioxide/Reduced Graphene Oxide Nanocomposites as Anode Materials for High-performance Lithium ion Batteries. *J. Power Sources* **2016**, *312*, 207−215.
(10) Fan, X.; Li, S.; Lu, L. Porous Micrometer-sized MnO Cubes as Anode of Lithium Ion Battery. *Electrochim. Acta* **2016**, *200*, 152−160.
(11) Zhao, D.; Qin, J. W.; Zheng, L. R.; Cao, M. H. Amorphous Vanadium Oxide/Molybdenum Oxide Hybrid with Three Dimensional Ordered Hierarchically Porous Structure as a High-performance Li-ion Battery Anode. *Chem. Mater.* **2016**, *28* (12), 4180−4190.
(12) Li, X.; Meng, X.; Liu, J.; Geng, D.; Zhang, Y.; Banis, M. N.; Li, Y.; Yang, J.; Li, R.; Sun, X.; Cai, M.; Verbrugge, M. W. Tin Oxide with Controlled Morphology and Crystallinity by Atomic Layer Deposition onto Graphene Nanosheets for Enhanced Lithium Storage. *Adv. Funct. Mater.* **2012**, *22* (8), 1647−1654.
(13) Wang, X. L.; Han, W. Q.; Chen, H.; Bai, J.; Tyson, T. A.; Yu, X. Q.; Wang, X. J.; Yang, X. Q. Amorphous Hierarchical Porous GeO_x as High-capacity Anodes for Li ion Batteries with very Long Cycling Life. *J. Am. Chem. Soc.* **2011**, *133* (51), 20692−20695.
(14) Chae, C.; Kim, J. H.; Kim, J. M.; Sun, Y.-K.; Lee, J. K. Highly Reversible Conversion-capacity of MnO_x-loaded Ordered Mesoporous Carbon Nanorods for Lithium-ion Battery Anodes. *J. Mater. Chem.* **2012**, *22* (34), 17870−17877.
(15) Guo, J. C.; Liu, Q.; Wang, C. S.; Zachariah, M. R. Interdispersed Amorphous MnO_x-carbon Nanocomposites with Superior Electrochemical Performance as Lithium-storage Material. *Adv. Funct. Mater.* **2012**, *22* (4), 803−811.
(16) Chae, C.; Park, H.; Kim, D.; Kim, J.; Oh, E.-S.; Lee, J. K. A Li-ion Battery Using $LiMn_2O_4$ Cathode and MnO_x/C Anode. *J. Power Sources* **2013**, *244*, 214−221.
(17) Qin, J.; Zhang, Q.; Cao, Z.; Li, X.; Hu, C.; Wei, B. MnO_x/SWCNT Macro-films as Flexible Binder-free Anodes for High-performance Li-ion Batteries. *Nano Energy* **2013**, *2* (5), 733−741.
(18) Wu, D.; Yang, R.; Sun, Q.; Shen, L.; Ji, W.; Shen, R.; Jiang, M.; Ding, W.; Peng, L. Simple Synthesis of TiO_2/MnO_x Composite with Enhanced Performances as Anode Materials for Li-ion Battery. *Electrochim. Acta* **2016**, *211*, 832−841.
(19) Pang, H.; Yang, Z.; Lv, J.; Yan, W.; Guo, T. Novel MnO_x@Carbon Hybrid Nanowires with Core/Shell Architecture as Highly Reversible Anode Materials for Lithium ion Batteries. *Energy* **2014**, *69*, 392−398.
(20) Lin, X. R.; Salari, M.; Arava, L. M. R.; Ajayan, P. M.; Grinstaff, M. W. High Temperature Electrical Energy Storage: Advances, Challenges, and Frontiers. *Chem. Soc. Rev.* **2016**, *45* (21), 5848−5887.
(21) Rao, Z. H.; Wang, S. F. A Review of Power Battery Thermal Energy Management. *Renew. Sust. Energy. Rev.* **2011**, *15* (9), 4554−4571.
(22) Li, S. Z.; Li, Q. Y.; Carpick, R. W.; Gumbsch, P.; Liu, X. Z.; Ding, X. D.; Sun, J.; Li, J. The Evolving Quality of Frictional Contact with Graphene. *Nature* **2016**, *539* (7630), 541−545.
(23) Posudievsky, O. Y.; Khazieieva, O. A.; Koshechko, V. G.; Pokhodenko, V. D. Preparation of Graphene Oxide by Solvent-free Mechanochemical Oxidation of Graphite. *J. Mater. Chem.* **2012**, *22* (25), 12465−12467.
(24) White, W. B.; Keramidas, V. G. G. K eramidas., Vibrational Spectra of Oxides with The C-type Rare Earth Oxide Structure. *Spectrochim. Acta Part A Mol. Spectrosc* **1972**, *28*, 501−509.
(25) Buciuman, F.; Patcas, F.; Craciun, R.; Zahn, D. R. T. Vibrational Spectroscopy of Bulk and Supported Manganese Oxides. *Phys. Chem. Chem. Phys.* **1999**, *1*, 185−190.
(26) Khan, U.; O'Neill, A.; Lotya, M.; De, S.; Coleman, J. N. High-concentration Solvent Exfoliation of Graphene. *Small* **2010**, *6* (7), 864−871.
(27) Park, K. H.; Lee, D.; Kim, J.; Song, J.; Lee, Y. M.; Kim, H. T.; Park, J. K. Defect-free, Size-tunable Graphene for High-performance Lithium Ion Battery. *Nano Lett.* **2014**, *14* (8), 4306−4313.
(28) Paton, K. R.; Varrla, E.; Backes, C.; Smith, R. J.; Khan, U.; O'Neill, A.; Boland, C.; Lotya, M.; Istrate, O. M.; King, P.; Higgins, T.; Barwich, S.; May, P.; Puczkarski, P.; Ahmed, I.; Moebius, M.; Pettersson, H.; Long, E.; Coelho, J.; O'Brien, S. E.; McGuire, E. K.; Sanchez, B. M.; Duesberg, G. S.; McEvoy, N.; Pennycook, T. J.; Downing, C.; Crossley, A.; Nicolosi, V.; Coleman, J. N. Scalable Production of Large Quantities of Defect-Free Few-layer Graphene by Shear Exfoliation in Liquids. *Nat. Mater.* **2014**, *13* (6), 624−630.
(29) Yang, H.; Jiang, J.; Zhou, W.; Lai, L.; Xi, L.; Lam, Y. M.; Shen, Z.; Khezri, B.; Yu, T. Influences of Graphene Oxide Support on the Electrochemical Performances of Graphene Oxide-MnO_2 Nanocomposites. *Nanoscale Res. Lett.* **2011**, *6* (1), 531.
(30) Perego, M.; Molle, A.; Fanciulli, M. Effect of Oxygen on The Electronic Configuration of Gd_2O_3/Ge Heterojunctions. *Appl. Phys. Lett.* **2008**, *92* (4), 042106.
(31) Sun, Y.; Hu, X.; Luo, W.; Huang, Y. Porous Carbon-modified MnO Disks Prepared by a Microwave-polyol Process and their Superior Lithium-ion Storage Properties. *J. Mater. Chem.* **2012**, *22* (36), 19190.
(32) Liu, C.; Zhang, C.; Song, H.; Zhang, C.; Liu, Y.; Nan, X.; Cao, G. Mesocrystal MnO Cubes as Anode for Li-ion Capacitors. *Nano Energy* **2016**, *22*, 290−300.
(33) Zhong, K.; Zhang, B.; Luo, S.; Wen, W.; Li, H.; Huang, X.; Chen, L. Investigation on Porous MnO Microsphere Anode for Lithium Ion Batteries. *J. Power Sources* **2011**, *196* (16), 6802−6808.
(34) Park, H.; Choi, S.; Lee, S.-J.; Cho, Y.-G.; Hwang, G.; Song, H.-K.; Choi, N.-S.; Park, S. Design of an Ultra-durable Silicon-based Battery Anode Material with Exceptional High-temperature Cycling Stability. *Nano Energy* **2016**, *26*, 192−199.
(35) Mao, L. P.; Li, B. C.; Cui, X. L.; Zhao, Y. Y.; Xu, X. L.; Shi, X. M.; Li, S. Y.; Li, F. Q. Electrochemical Performance of Electrolytes Based upon Lithium Bis(Oxalate)Borate and Sulfolane/Alkyl Sulfite Mixtures for High Temperature Lithium-ion Batteries. *Electrochim. Acta* **2012**, *79*, 197−201.
(36) Haruta, M.; Okubo, T.; Masuo, Y.; Yoshida, S.; Tomita, A.; Takenaka, T.; Doi, T.; Inaba, M. Temperature Effects on SEI Formation and Cyclability of Si Nanoflake Powder Anode in the Presence of SEI-forming Additives. *Electrochim. Acta* **2017**, *224*, 186−193.
(37) Lu, X.; Wang, R.; Bai, Y.; Chen, J.; Sun, J. Facile Preparation of a Three-dimensional Fe_3O_4/Macroporous Graphene Composite for Highperformance Li Storage. *J. Mater. Chem. A* **2015**, *3*, 12031−12037.
(38) Du, Y.; Wu, S.; Huang, M.; Tian, X. Reduced Graphene Oxide-Wrapped Pyrite as Anode Materials for Li-Ion Batteries with Enhanced Long-Term Performance under Harsh Operational Environments. *Chem. Eng. J.* **2017**, *326*, 257−264.
(39) Du, Y.; Liu, C.; Sun, S.; Wu, S. Core-shell MnO@$MnFe_2O_4$ Anchored by Reduced Graphene Oxide as Anode of Li-Ion Batteries Operated under Ultrawide Temperature Range. *ChemElectroChem* **2017**, DOI: 10.1002/celc.201700527.
(40) Lu, M.; Liao, C.; Jiang, C.; Du, Y.; Zhang, Z.; Wu, S. Remarkable High-temperature Performance of Hollow Co_9S_8 Nanoparticles Integrated with Carbon Materials for Lithium-ion Batteries. *Electrochim. Acta* **2017**, *250*, 196−202.

DOI: 10.1021/acsami.7b09853
ACS Appl. Mater. Interfaces 2017, 9, 33896−33905

(41) Kang, D. M.; Liu, Q. L.; Si, R.; Gu, J. J.; Zhang, W.; Zhang, D. Crosslinking-derived MnO/Carbon Hybrid with Ultrasmall Nanoparticles for Increasing Lithium Storage Capacity during Cycling. *Carbon* **2016**, *99*, 138−147.
(42) Yu, Z.; Song, J.; Gordin, M. L.; Yi, R.; Tang, D.; Wang, D. Phosphorus-graphene Nanosheet Hybrids as Lithium-ion Anode with Exceptional High-temperature Cycling Stability. *Adv. Sci. (Weinh)* **2015**, *2* (1−2), 1400020.
(43) Guo, J.; Zuo, W.; Cai, Y.; Chen, S.; Zhang, S.; Liu, J. A Novel $Li_4Ti_5O_{12}$-Based High-Performance Lithium-ion Electrode at Elevated Temperature. *J. Mater. Chem. A* **2015**, *3* (9), 4938−4944.
(44) Ilango, P. R.; Prasanna, K.; Subburaj, T.; Jo, Y. N.; Lee, C. W. Facile Longitudinal Unzipping of Carbon Nanotubes to Graphene Nanoribbons and Their Effects on $LiMn_2O_4$ Cathodes in Rechargeable Lithium-ion Batteries. *Acta Mater.* **2015**, *100*, 11−18.
(45) Yuan, T.; Jiang, Y.; Sun, W.; Xiang, B.; Li, Y.; Yan, M.; Xu, B.; Dou, S. Ever-increasing Pseudocapacitance in RGO-MnO-RGO Sandwich Nanostructures for Ultrahigh-rate Lithium Storage. *Adv. Funct. Mater.* **2016**, *26* (13), 2198−2206.
(46) Zhang, J.; Zhang, W.; He, T.; Amiinu, I. S.; Kou, Z. K.; Li, J. N.; Mu, S. C. Smart Reconstruction of Dual-carbon Decorated MnO for Anode with High-capacity and Ultralong-life Lithium Storage Properties. *Carbon* **2017**, *115*, 95−104.
(47) Brezesinski, T.; Wang, J.; Tolbert, S. H.; Dunn, B. Ordered Mesoporous α-MoO_3 with Iso-oriented Nanocrystalline Walls for Thin-film Pseudocapacitors. *Nat. Mater.* **2010**, *9* (2), 146−151.
(48) Wang, J.; Tang, H.; Zhang, L.; Ren, H.; Yu, R.; Jin, Q.; Qi, J.; Mao, D.; Yang, M.; Wang, Y.; Liu, P.; Zhang, Y.; Wen, Y.; Gu, L.; Ma, G.; Su, Z.; Tang, Z.; Zhao, H.; Wang, D. Multi-shelled Metal Oxides Prepared via an Anion-adsorption Mechanism for Lithium-ion Batteries. *Nat. Energy* **2016**, *1* (5), 16050.
(49) Zhao, C.; Yu, C.; Zhang, M.; Huang, H.; Li, S.; Han, X.; Liu, Z.; Yang, J.; Xiao, W.; Liang, J.; Sun, X.; Qiu, J. Ultrafine MoO_2-carbon Microstructures Enable Ultralong-life Power-type Sodium Ion Storage by Enhanced Pseudocapacitance. *Adv. Energy. Mater.* **2017**, *7*, 1602880.
(50) Zhao, K. N.; Liu, F. N.; Niu, C. J.; Xu, W. W.; Dong, Y. F.; Zhang, L.; Xie, S. M.; Yan, M. Y.; Wei, Q. L.; Zhao, D. Y.; Mai, L. Q. Graphene Oxide Wrapped Amorphous Copper Vanadium Oxide with Enhanced Capacitive Behavior for High-Rate and Long-Life Lithium-Ion Battery Anodes. *Adv. Sci.* **2015**, *2* (12), 1500154.
(51) Chae, O. B.; Kim, J.; Park, I.; Jeong, H.; Ku, J. H.; Ryu, J. H.; Kang, K.; Oh, S. M. Reversible Lithium Storage at Highly Populated Vacant Sites in an Amorphous Vanadium Pentoxide Electrode. *Chem. Mater.* **2014**, *26* (20), 5874−5881.
(52) Wang, J.; Manga, K. K.; Bao, Q.; Loh, K. P. High-yield Synthesis of Few-layer Graphene Flakes through Electrochemical Expansion of Graphite in Propylene Carbonate Electrolyte. *J. Am. Chem. Soc.* **2011**, *133* (23), 8888−8891.
(53) Ciez, R. E.; Whitacre, J. F. Comparison between Cylindrical and Prismatic Lithium-ion Cell Costs Using a Process Based Cost Model. *J. Power Sources* **2017**, *340*, 273−281.

DOI: 10.1021/acsami.7b09853
ACS Appl. Mater. Interfaces 2017, 9, 33896−33905